RSC Advances

ROYAL SOCIETY
OF CHEMISTRY

www.rsc.org/advances

Size-dependent Ultrahigh Electrocaloric Effect near Pseudo-First-Order Phase Transition Temperature in Barium Titanate Nanoparticles

Hong-Hui Wu, Jiaming Zhu, and Tong-Yi Zhang*

Department of Mechanical and Aerospace Engineering, Hong Kong University of Science and Technology,
Clear Water Bay, Kowloon, Hong Kong, China

Abstract

The electrocaloric effect (ECE) of ferroelectric materials, which occurs significantly in a narrow temperature region near the first-order paraelectric/ferroelectric transition (FOPFT) Curie temperature, has great potential in solid-state refrigeration. Most ferroelectric materials, however, bear the second-order paraelectric/ferroelectric transition (SOPFT). In the present study, we demonstrate size-dependent pseudo-first-order phase transition (PFOPT), associated ultrahigh ECE and Curie temperature in ferroelectric nanoparticles with degradation layers by employing phase field modeling. The PFOPT behavior of the polarization component P_3 along the applied electric field direction x_3 versus temperature is similar to the classical FOPFT behavior. The results indicate that the ultrahigh ECE and PFOPT occur at temperatures below the Curie temperature of a given nanoparticle size. The adiabatic temperature change is 3.347 K in the simulated barium titanate nanoparticle of $10\times10\times8$ normalized size under 96.502 kV/cm applied electric field change. The concept of PFOPT should be general to be applied to all ferroelectric perovskite materials. Therefore, the current results provide a novel physical perspective for experiments and for lower power/higher efficient solid-state cooling devices.

---

*Corresponding author. Tel: +852 2358 7192, Fax: +852 2358-1543, E-mail address: mezhangt@ust.hk

Keywords: Size effect; Ultrahigh electrocaloric effect; Pseudo-first-order phase transition; Domain configuration; Degradation layers; Nanoparticles

1. Introduction

The electrocaloric (EC) effect, which refers to the change in adiabatic temperature of a ferroelectric by varying an applied electric field, in ferroelectric materials has attracted widespread interests due to the prospect of a novel approach to realize solid-state cooling devices instead of the existing vapor-compression refrigeration.[1-5] Although bulk ferroelectric (FE) ceramics at low electric fields produced only small changes in adiabatic temperature (ΔT<2 K) at temperatures near the Curie temperature T_c, an adiabatic temperature change (ATC) of ΔT=12 K was observed under applied 776 kV/cm at 226 ℃ in a 350 nm $PbZr_{0.95}Ti_{0.05}O_3$ thin film prepared by a sol-gel method,[6] and an ATC of 5 K in a 260 nm thick relaxor ferroelectric thin film[7] $0.9PbMg_{1/3}Nb_{2/3}O_3$-$0.1PbTiO_3$ (PMN-PT) at 895 kV/cm and 75 ℃. After that, the large EC effect has been observed in other ferroelectric and antiferroelectric systems, relaxor and polymer films.[8-13] The ATC in ferroelectric thin films is greatly enhanced by varying electric field from zero to ultrahigh fields of hundreds kV/cm due to the enhanced breakdown strengths of the materials in thin films compared to their bulk counterparts, whereas the associated electrocaloric strength (ECS) $|\Delta T|/|\Delta E|$ is even lower than that of the bulk counterparts.[14-16] The ECE of ferroelectrics intrinsically stems from the temperature dependence of polarization, an applied electric field can reversibly change the temperature of an electrocaloric material under adiabatic condition, and the effect becomes strongest near the FOPFT point. In principle, Landau-Devonshire theory describes the thermodynamic behaviors of ferroelectric materials including FOPFT and the free energy as a function of polarization and the relationship between electric field and polarization at various temperatures.[17,18] As a typical example, Fig. 1 plots the one-dimensional Landau-Devonshire free energy and electric field versus polarization at four characteristic temperatures during the phase transition process, i.e. Curie-Weiss temperature T_0, Curie temperature T_{c}, ferroelectric limit temperature T_1 and limit temperature of electric field-induced phase transition T_2, where the $BaTiO_3$ material properties are used[19] and the dotted parts of the curves correspond to the unstable state. At the Curie-Weiss temperature T_0 shown in Fig. 1(a), the regular polarization versus electric field (P-E) hysteresis loop appears as the consequence of the double-wells-free energy profile. When the temperature increases to the Curie temperature T_{c}, the three-wells-function of Landau-Devonshire free energy leads to the critical P-E hysteresis loop amid regular shape and a double-hysteresis loop, as shown in Fig. 1(b). At the ferroelectric limit temperature T_1 shown in Fig. 1(c), the double-hysteresis loop occurs with the unequal three-wells-free energy function. This double-hysteresis loop originates from a typical electric-field-induced phase transition from paraelectric phase to ferroelectric phase. At the limit temperature of field-induced phase transition T_2, as shown in Fig. 1(d), the double-hysteresis loop disappears and a quasi-linear P-E curve emerges, indicating the crystal is paraelectric and cannot be transformed into ferroelectric phase within the range of applied electric field.

The first-order phase transition Curie temperature is the natural hub to generate significant ATC and ECS, which has been proved by many experimental and theoretical studies.[16,20-24] For example, Moya et al.[16] presented direct measurements of ΔT in single crystal $BaTiO_3$ near the Curie temperature T_{c} and observed the giant ECS $|\Delta T|/|\Delta E|$ of 0.22 $\mathrm{K \cdot cm/kV}$. Li et al.[20] also directly measured ECE in an irradiated poly(inylidenefluoride-trifluoroethylene) 65/35 mol. % copolymer. Their experimental results show that near the FOPFT temperature, the applied $\Delta E = 180$ MV/m causes an isothermal entropy change $\Delta S_{\text{int}} = 160\ \text{JKg}^{-1}\text{K}^{-1}$ and an ATC ΔT_{int} =35 K. By employing molecular dynamics with a first-principles-based shell model potential, Rose *et al.*[21] found a giant ATC $\Delta T \sim 25\,\text{K}$ in lithium niobate ($LiNbO_3$) under ΔE =75 MV/m through the FOPFT temperature and suggested that the operating temperature for refrigeration and energy scavenging applications should be above the FOPFT temperature to obtain a large electrocaloric response. Thermodynamic analysis indicates that giant EC effect $\Delta T \sim 1.6\,\text{K}$ under ΔE =100 kV/cm observed in perovskite $BaTiO_3$ bulk single crystal[22] is attributed to the intrinsic monodomain thermodielectric properties when driven near the curie temperature by sufficiently high electric field. Using a phase field model, Wang *et al.*[23] showed that the extrinsic mechanical contribution from the multidomain to monodomain transition significantly enhanced the EC response in $PbTiO_3$ crystals around the Curie temperature. Recently, a giant EC strength of 0.48 $\text{K}\cdot\text{cm/kV}$ was found in $BaTiO_3$ single crystal under applied electric field ΔE =10 kV/cm near the FOPFT temperature.[24] But, such large ECS was not stable after tenfold thermal and electrical cycles because the field-induced phase transition and domain switching resulted in numerous defects such as microcracks. Clearly, defects may play important roles in the electrocaloric effect, which has not been studied systematically so far.

The depolarization field in low-dimensional ferroelectrics becomes stronger in comparison with that in the counterpart bulks and thus may alter the domain structure, phase transition temperature, switchability as well as electrocaloric properties. Extensive ECE studies[6-13] have carried out on ferroelectric thin films because films survive under high electric field. The previous study indicates the thickness-dependent ECE.[25] There are, however, rare reports in the literature about the ECE investigation on ferroelectric nanoparticles, although free-standing[26-28] and epitaxial growth[29-32] ferroelectric nanoparticles have been successfully fabricated in experiments and these nanoparticles have the great application potential in fabricating nanoscale ECE cooling devices. Differing from two-dimensional ferroelectric thin films, the unique geometry of ferroelectric nanoparticles provides special interaction among the size, depolarization field, temperature, electric field and spontaneous polarization. The unique geometry of ferroelectric nanoparticles results in distinctive polarization structure, and hence the exceptional ECE behavior. In the present work, we conduct phase field simulations and take lead-free $BaTiO_3$ nanoparticles as an example to illustrate the exceptional ECE behavior. Experimental observations and theoretical studies have proved the presence of a degradation layer between a metallic electrode and the ferroelectric material.[33-35] The degradation layer is considered here, which other defects such as vacancies[36,37] and dislocations[38-40] *etc.* are excluded from the present work.

2. Methodology

Polarization $\mathbf{P} = (P_1, P_2, P_3)$ is used as the order parameter in the Ginzburg-Landau-Devonshire theory based phase field simulations. The phase transition and domain evolution are a direct consequence of the minimization process of the total free energy over the whole system. The total free energy of ferroelectrics is obtained by integrating an electrical enthalpy density over the whole system,[41,42]

$$F = \int_{\Omega} f\, dV \tag{1a}$$

$$\begin{aligned} f\left(P_i, P_{i,j}, \varepsilon_{ij}, E_i\right) = {} & \alpha_i P_i^2 + \alpha_{ij} P_i^2 P_j^2 + \alpha_{ijk} P_i^2 P_j^2 P_k^2 + \alpha_{ijkl} P_i^2 P_j^2 P_k^2 P_l^2 \\ & + \frac{1}{2} c_{ijkl} \varepsilon_{ij} \varepsilon_{kl} - q_{ijkl} \varepsilon_{ij} P_k P_l + \frac{1}{2} g_{ijkl} P_{i,j} P_{k,l} - \frac{1}{2} \varepsilon_r \varepsilon_0 E_i E_i - E_i P_i \end{aligned} \quad (i, j, k, l = 1, 2, 3) \tag{1b}$$

In Eq. (1b), the first four terms represent the Landau-Devonshire energy density, where α_i is the dielectric stiffness, which is directly related to temperature by $\alpha_1 = (T - T_0)/2\varepsilon_0 C_0$, T and T_0

signify temperature and the Curie-Weiss temperature, respectively, C_0 is the Curie constant, and ε_0 is the dielectric constant of vacuum. α_{ij}, α_{ijk} and α_{ijkl} are higher order dielectric stiffnesses. The fifth term indicates the mechanical energy density, where ε_{ij} and c_{ijkl} are the strains and elastic constants, respectively. The sixth term represents the coupling energy density between the polarization and elastic deformation, where q_{ijkl} is the electrostrictive coefficient. The seventh term is the gradient energy density, where g_{ijkl} is the gradient coefficient and $P_{i,j}$ denotes the spatial derivative of the i th component of the polarization vector, P_i, with respect to the j th coordinate. The gradient energy density gives the energy penalty for spatially inhomogeneous polarization. The last two terms are the electric energy density due to the presence of electric field, in which ε_r is the background dielectric constant of the material and E_i is the electric field. With the electrical enthalpy density of Eq. (1), the stresses and electric displacements can be derived as $\sigma_{ij} = \partial f / \partial \varepsilon_{ij}$ and $D_i = -\partial f / \partial E_i$ respectively. Voigt notation is adopted here to express the electrostrictive coefficient q_{ijkl}, the gradient coefficient g_{ijkl}, and the elastic constants c_{ijkl}. Table 1 shows the values[45] of the normalized material coefficients of $BaTiO_3$ employed in the simulations.

In the phase field model, the polarization switching process is determined by the following time-dependent Ginzburg-Landau equation,

$$\frac{\partial P_i(\mathbf{x},t)}{\partial t} = -L \frac{\delta F}{\delta P_i(\mathbf{x},t)} \tag{2}$$

where L is the kinetic coefficient, the variation of $\frac{\delta F}{\delta P_i(\mathbf{x},t)}$ on the right hand side of Eq. (2) represents the thermodynamic driving force for the spatial and temporal evolution of domain structures. $\mathbf{x} = (x_1, x_2, x_3)$ denotes the spatial vector and t is time. In addition to Eq. (2), the mechanical and electrical equilibrium equations of $\sigma_{ij,j} = 0$ and $D_{i,i} = 0$ must be satisfied at the same time for charge-free and body force-free ferroelectric materials. In the numerical calculations of Eq. (2), the finite element method with eight-node brick elements and seven degrees of freedom at each node is employed for the space discretization, and the backward Euler iteration method is adopted for the time integration.

The electrocaloric effect is the temperature change of a crystal caused by an adiabatic change in an applied electric field. The isothermal entropy change ΔS and ATC ΔT as the applied electric field change from an initial value E_α of to a final value of E_β are calculated from,[1]

$$\begin{aligned} \Delta S &= -\int_{E_\alpha}^{E_\beta} \left(\frac{\partial P_i}{\partial T} \right)_{E_i} dE_i \\ \Delta T &= -\int_{E_\alpha}^{E_\beta} \frac{T}{C\rho} \left(\frac{\partial P_i}{\partial T} \right)_{E_i} dE_i \end{aligned} \tag{4}$$

where $C\rho$ is the specific heat capacity per unit volume.

Fig. 2 is a schematic drawing of the phase field model for a $BaTiO_3$ nanoparticle. The top and bottom of the nanoparticle are covered by metal electrodes, cross which an alternating electric field is applied. To consider the material degradation at the electrode-ferroelectrics interface, two degradation layers also called deadlayer[33-35] at the upper and lower interfaces between the ferroelectric and electrode are included in the present model, due to the existence of top and bottom dead layers, the ferroelectric nanoparticle is close to an open-circuit boundary condition. In the numerical treatment, degradation layers are set to be dielectric material without spontaneous polarization. Thus $\mathbf{P} = 0$ is used as the boundary condition along the interfaces between the electrode and the ferroelectric nanoparticle. The length and width of the nanoparticles are the same and maintained at 10nm in the present work and the height of the nanoparticles is allowed to change, ranging from 2 nm to 8 nm, to study the height dependent behavior. For convenience, dimensionless material parameters with superscript * are used in the numerical calculations, while temperature, ATC and instant ECS are given in the real physical dimensions in order to compare with the reported experimental results. The electrical boundary condition along x_1 and x_2 directions are open circuit, and mechanical boundary conditions of all directions are traction-free. The initial state of spontaneous polarization in the simulated cell was achieved by applying zero electric potential on the two electrodes, and a uniform random distribution of initial dimensionless polarizations with the maximum magnitude less than 0.005 was used to trigger the polarization evolution, which led to a stable domain structure after 50000 adaptive step increments. Then, an alternating electric voltage $\varphi^{ex,*} = \varphi_0^* \sin(2.5\pi\tau/125000)$ was applied across the electrodes, where τ was integer to denote the time step. Under each applied electric field at a given time step τ, the simulated ferroelectric nanoparticle was allowed to evolve once with a dimensionless time step of $\Delta t^* = 0.04$. The average polarization along the electric field direction was taken as the macroscopic response of the simulated system. The values of $P_3^*(T)$ were extracted from the upper branches of P-E hysteresis loops in $E_3^* > 0$. The maximum normalized electric field $E_3^* = 1.0$, corresponding to the electric field E_3 = 96.502 kV/cm, and following the previous work,[6,22,35,43,44] the absolute value of the heat capacity $C\rho = 3.05\times10^6$ J/Km is assumed as a constant in the present calculation. In the present phase field simulations, the Curie temperature was defined as the minimum temperature at which the spontaneous polarization **P** becomes zero, while the Pseudo first-order phase transition (PFOPT) point is defined as the minimum temperature at which the polarization P_3 becomes zero. Clearly, the PFOPT temperature is just based on the behavior of the component of polarization P_3 along the direction of applied electric field x_3, regardless of the other components of spontaneous polarization that may still have finite nonzero values.

3. Results and discussion

3.1. Size-dependent PFOPT behavior of the $BaTiO_3$ nanoparticles

Fig. 3(a) gives the hysteresis loops for the nanoparticles with different heights at room temperature, indicating that coercive field and remnant polarization are reduced with the decrease of the nanoparticle height. Interestingly, once the height of the nanoparticle drops to 2 at temperature 298 K, a double hysteresis loop appears which is usually observed around the Curie temperature of FOPFT point, and accompanied by large electrocaloric effect.[16,20-24] Fig. 3(b) shows the hysteresis loops of the nanoparticles with different heights at 331 K, illustrating that both coercive field and remnant polarization shrink in with the height decrease. Furthermore, for heights $H^*=3$ and $H^*=4$, the P-E curves exhibit the double hysteresis loop with low remnant polarizations of 7.41×10^{-4} and 0.097, respectively. Fig. 3(c) illustrates the remnant polarization $P_3^{r,*}$ versus temperature, indicating that the remnant polarization of the $H^*=2$ nanoparticle remains zero in the temperature range from 273 K to 313 K, during which the double hysteresis loops appear in the $H^*=3$ nanoparticle. The traditional FOPFT point occurs at the Curie temperature, at which the spontaneous polarization **P** jumps from a finite value in the ferroelectric phase to zero in the paraelectric phase. As shown in Fig. 3(c), the remnant polarization drops steeply in a certain temperature range as the temperature increases, similarly to the polarization versus temperature drop in the FOPFT process, thereby called PFOPT. The PFOPT occurs in a nanoparticle at a temperature below the Curie temperature of the nanoparticle. Caution must be used here because the Curie temperature of a nanoparticle varies with the particle height. Take the $H^*=4$ nanoparticle for example, the PFOPT point takes place around the temperature 333 K, while its Curie temperature still remains at 348 K. Among the temperature range from 333 K to 348 K, P_3 disappears, but the polarizations P_1 and P_2 still have finite nonzero values. Fig. 3(d) illustrates the height dependence of the Curie and PFOPT temperatures of those nanoparticles. When the nanoparticle height increases, the difference between the Curie and PFOPT temperatures becomes smaller and both Curie and PFOPT temperatures increase and approach to the intrinsic Curie temperature 398 K of the $BaTiO_3$ bulk counterpart, because the charge screening role from the degradation layers diminishes gradually.

Fig. 4 gives the domain structures corresponding to the remnant polarizations indicated in Fig. 3(b). Fig. 4 (a) shows a typical vortex structure on x_1-x_2-plane for the $H^* = 3$ nanoparticle. The appearance of vortex structure, as a result of the dielectric shielding by degradation layers and the traction-free surfaces, significantly reduces the depolarization energy by arranging polarizations head-to-tail within the x_1-x_2-plane. The in-plane vortex structure explains why the remnant polarization $P_3^{r,*}$ is near zero when the temperature T is lower than the Curie temperature. When the height increases to 4, a double vortex structure forms on the lateral sides of the nanoparticle and thus gives a limited net remnant polarization $P_3^{r,*}$=0.097 along x_3 direction. The relatively high remnant polarizations (c) and (d) shown in Fig. 3(b) stem from the almost perfect monodomain structure due to the gradual decrease of dielectric shielding ability by the degradation layers, as shown in Fig. 4 (c) and Fig. 4 (d).

3.2. Hysteresis behavior and corresponding domain structure of a representative nanoparticle

The performance of ferroelectricity in the $H^* = 5$ nanoparticle deteriorates as temperature increases from 298 K to 363 K, as shown in Fig. 5. An unusual double hysteresis loop starts to form at 353 K, which leads to the steep drops of both remnant polarization and coercive field to zero. Such a temperature-dependent behavior causes giant ATC, even at low electric field. Fig. 5(b) gives the curves of polarization P_3^* versus temperature at various applied electric fields and the inset presents the corresponding $\left(dP_3^*/dT\right)_{\mathrm{E}}$. The remnant polarization decreases rapidly from 0.557 to 0.0211 as temperature 343 K increases by only 4 K to 347 K. The peak $\left(dP_3^*/dT\right)_{\mathrm{E}}$ temperature rises from 345 K to 353 K, 361 K, and 371 K, respectively, as the applied electric field increases to E_3^*=0.1, E_3^*=0.2 and E_3^*=0.3. However, the peak of $\left(dP_3^*/dT\right)_{\mathrm{E}}$ becomes blurred when the applied electric field further increases to E_3^*=0.4 and above.

Figs. 6(a1)-(a4) show the domain structures of the $H^* = 5$ nanoparticle at temperature 323 K corresponding to the points (a1)-(a4) in Fig. 5(a). All polarizations in the nanoparticle are along one direction at the maximum applied electric field E_3^*=1.0. When the applied electric field reduces to zero, as shown in Fig. 6(a2), the monodomain structure survives with the decrease in the polarization P_3 magnitude. Around the coercive field, as shown in Fig. 6(a3) at the applied electric field -0.279, the vortex structure forms in the nanoparticle. Further increasing the field absolute strength to -0.294, the polarization-downward monodomain structure appears, as shown in Fig. 6(a4). The simulation result indicates that the domain switching from polarization-upward monodomain structure to vortex structure and then to polarization-downward monodomain structure happens within a relatively narrow range of electric field near the coercive field and the vortex structure is only an intermediate structure on the pathway during the domain switching. The intermediate structure changes with temperature. Figs. 6(b1)-(b4) present the domain structures at 353 K corresponding to the points (b1)-(b4) in Fig. 5(a). Again Fig. 6(b1) is a single domain with all polarization along the applied electric direction under E_3^*=1.0. The polarization in Fig. 6(b2) forms a vortex domain structure on the x_1-x_2-plane, without any net polarization left along the x_3 direction. As the applied electric field decreases to -0.218, the vortex structure is unstable that polarizations rotate and switch in order to align themselves along the electric field direction for energy minimization. When the negative electric field increases to -0.234, all polarizations are parallel to the applied electric field direction, resulting in a single domain structure. The in-plane vortex structure at remnant polarization shown in Fig. 6(b2) is induced by the depolarization effect of the degradation layers, while the in-plane vortex structure in Fig. 6(a3) at the applied electric field E_3^*=-0.279 is caused by the external electric field-induced phase transition, which is a transitional configuration during the domain reversal. The rich intermediate polarization structure might indicate high entropy in the nanoparticle, which will bring a giant ECE.

3.3. Size-dependent ATC and instant EC strength of the nanoparticles

Figs. 7(a)-(d) give the ATC ΔT versus the initial temperature at various applied electric fields, respectively, for the H^*=4, 5, 7, and 8 nanoparticles. Fig. 7(a) shows that the ATC for the H^*=4 nanoparticle reaches the first peak of ΔT =2.678 K under ΔE_3^*=1.0 at 331 K, which is 34 K lower than its Curie temperature 365 K. The result implies that the ATC peak can be tuned to a much lower temperature. With the temperature increases to its Curie temperature, the ΔT still remains a high value of 2.073 K under $\Delta E_3^* = 1.0$. As expected, the ATC ΔT increase monotonically with the increasing of ΔE_3^*. The ATC ΔT in the $H^* = 5$ nanoparticle shown in Fig. 7(b) is similar to that in Fig. 7(a), with the first peak value of ΔT =2.933 K under $\Delta E_3^* = 1.0$ at 346 K. Fig. 7(c) indicates the first peak of ΔT =3.294 K in the $H^* = 7$ nanoparticle at 363 K under $\Delta E_3^* = 1.0$, while Fig. 7(d) illustrates the first peak of ΔT =3.347 K in the $H^* = 8$ nanoparticle at 373 K under $\Delta E_3^* = 1.0$. The results clearly imply that a higher value of the height yields a higher value ΔT at a higher temperature. The degradation layers generate the depolarization effect on the surfaces of the nanoparticles, which makes the generalized polarization along the x_3 direction smaller. The higher the height is, the weaker the depolarization effect and the higher the generalized polarization along the x_3 direction will be. A higher generalized polarization along the x_3 direction has a larger capacity to change its magnitude by an applied electric field, which in turn can produce a higher change in adiabatic temperature. For comparison, the intrinsic ATC of ΔT =3.891 K under $\Delta E_3^* = 1.0$ in BaTiO$_3$ bulk single crystal is calculated by phase field simulation,[46] which should be the saturation limit with the further increase of the nanoparticle height. Despite the ATC ΔT induced by the PFOPT is slightly smaller than the intrinsic ATC ΔT at FOPFT, the lower temperature of PFOPT makes it competitive to the FOPFT. Besides, the PFOPT concept can be applied to the ferroelectric perovskite materials without the first-order paraelectric/ferroelectric transition and thus will greatly promote the application of ferroelectric nanoparticles in the next generation of solid-state cooling devices. Obviously, a great change in applied electric field achieves a large ATC ΔT. But, too high applied electric field brings two potential problems. One is the high applied electric field will cause large energy consumption and the other is the possibility of dielectric breakdown of ferroelectric ceramic/thin film/capacitor will be much higher. Therefore, the present finding that a change in relatively low electric field can also achieve a large ATC ΔT has considerably reduced or completely avoided the two potential problems. Figs. 8(a)-(d) show the instant ECSs $\left(dT/dE_3^*\right)_S$ versus electric field at different temperatures for the nanoparticles of H^* =4, 6, 7, and 8, respectively. At temperature 298 K, the instant ECS $\left(dT/dE_3^*\right)_S$ in the $H^* = 4$ nanoparticle is almost zero at an applied electric field E_3^* ranging from zero to 1.0, as shown in Fig. 8(a), while at temperature 330 K, a peak of $\left(dT/dE_3^*\right)_S$ =0.743 K$\cdot$cm/kV occurs at E_3^*= 0.0157, as marked by point (a2). As temperature further increases to T =343 K and T =365 K, the peak values decreased to $\left(dT/dE_3^*\right)_S$ =0.143 K$\cdot$cm/kV at point (a3) and $\left(dT/dE_3^*\right)_S$ =0.0719 K$\cdot$ cm/kV at point (a4), respectively, shifting to higher applied electric fields E_3^* =0.156 and 0.264. This result indicates that most efficient ATC electric field (or temperature) can be tuned by temperature (or electric field). The similar behavior of the instant ECS as described above for the H^*=4 nanoparticle is also observed for the nanoparticles with H^*=5, 7, and 8 with the first peaks (b2), (c2) and (d2) shifting to higher temperatures of 345 K, 362 K, and 367 K, respectively. The exciting simulation result will provide a clue to further ECE experiment.

4. Conclusions

In summary, the ECE in $BaTiO_3$ nanoparticles with degradation layers has been theoretically investigated by phase field simulations. The simulation results exhibit the size dependent ultrahigh electrocaloric effect occurring at temperatures lower than the Curie temperature of the nanoparticle. The PFOPT is defined based on the behavior of the polarization component P_3 along the applied electric field direction x_3 versus temperature under the charge screening of the degradation layers and the traction-free boundary condition along the nanoparticle surfaces. The double P-E hysteresis loops are accompanied with the PFOPT, and large ATC and ultrahigh instant ECS are achieved by a change in the applied electric field near the PFOPT temperature. The double hysteresis loops are manifested by the domain switching from upward monodomain structure to vortex domain structure to downward monodomain structure. The vortex domain structure possesses more entropy in compared to the monodomain structure, thereby giving an electric field induced isothermal entropy change. The simulations show also the interplay among the electric field, temperature, nanoparticle height, and polarization. It is the interplay that varies the most efficient ATC and instant ECS to occur at different temperature, electric field, and nanoparticle height. The present findings imply that it is possible to accomplish engineering feasible ECE at relatively low electric field, thereby leading to a new strategy to tailor ferroelectric materials and to improve the electrocaloric properties.

Acknowledgments

This work was supported by the Hong Kong Research Grants Council under the General Research Fund, 622813.

References

1 M. E. Lines and A. M. Glass, Oxford University Press, Clarendon, 1977.

2 J. D. Childress, *J. Appl. Phys.*, 1962, **33**, 1793.

3 G. G. Wiseman and J. K. Kuebler, *Phys. Rev.*, 1963, **131**, 2023.

4 G. Lombardo and R. O. Pohl, *Phys. Rev. Lett.*, 1965, **15**, 291-293.

5 P. D. Thacher, *J. Appl. Phys.*, 1968, **39**, 1996.

6 A. S. Mischenko, Q. Zhang, J. F. Scott, R. W. Whatmore and N. D. Mathur, *Science*, 2006, **311**, 1270-1271.

7 B. Neese, B. Chu, S. G. Lu, Y. Wang, E. Furman and Q. M. Zhang, *Science*, 2008, **321**, 821-823.

8 A. S. Mischenko, Q. Zhang, R. W. Whatmore, J. F. Scott and N. D. Mathur, *Appl. Phys. Lett.*, 2006, **89**, 242912.

9 B. Neese, S. G. Lu, B. Chu and Q. M. Zhang, *Appl. Phys. Lett.*, 2009, **94**, 042910.

10 H. Chen, T. L. Ren, X. M. Wu, Y. Yang and L. T. Liu, *Appl. Phys. Lett.*, 2009, **94**, 182902.

11 J. Hagberg, A. Uusimaki and H. Jantunen, *Appl. Phys. Lett.*, 2008, **92**, 132909.

12 S. G. Lu, B. Rožič, Q. M. Zhang, Z. Kutnjak and B. Neese, *Appl. Phys. Lett.*, 2011, **98**, 122906.

13 T. M. Correia, J. S. Young, R. W. Whatmore, J. F. Scott, N. D. Mathur and Q. Zhang, *Appl. Phys. Lett.*, 2009, **95**, 182904.

14 Y. Bai, K. Ding, G. P. Zheng, S. Q. Shi, J. L. Cao and L. J. Qiao, *AIP Adv.*, 2012, **2**, 022162.

15 Y. Bai, K. Ding, G. P. Zheng, S. Q. Shi and L. J. Qiao, *Phys. Status Solidi A*, 2012, **209**, 941-944.

16 X. Moya, E. Stern-Taulats, S. Crossley, D. González-Alonso, S. Kar-Narayan, A. Planes, L. Mañosa and N. D. Mathur, *Adv. Mater.*, 2013, **25**, 1360-1365.

17 W. J. Merz, *Phys. Rev.* 1953, **91**, 513.

18 Y. L. Li, L. E. Cross and L. Q. Chen, *J. Appl. Phys.*, 2005, **98**, 064101.

19 Landau-Devonshire free energy function $f(P,E)=\alpha_1 P^2+\alpha_{11}P^4+\alpha_{111}P^6+\alpha_{1111}P^8-E\ P$, where the normalized coefficient $\alpha_1=(T\text{-}388)/90$, $\alpha_{11}=-0.38193$, $\alpha_{111}=0.15932$, $\alpha_{1111}=0.32152$. The relationship between applied electric field *E* and polarization *P* can be obtained by $\partial f(P,E)/\partial P=0$.

20 X. Li, X. S. Qian, H. Gu, X. Chen, S. G. Lu, M. Lin, F. Bateman and Q. M. Zhang, *Appl. Phys. Lett.*, 2012, **101**, 132903.

21 M. C. Rose and R. E. Cohen, *Phys. Rev. Lett*., 2012, **109**, 187604.

22 G. Akcay, S. P. Alpay, J. V. Mantese and G. A. Rossetti, *Appl. Phys. Lett*., 2007, **90**, 252909.

23 J. Wang, M. Liu, Y. Zhang, T. Shimada, S. Shi and T. Kitamura, *J. Appl. Phys.*, 2014, **115**, 164102.

24 Y. Bai, X. Han, X. C. Zheng and L. Qiao, *Sci Rep.*, 2013, **3**, 2895.

25 J. H. Qiu and Q. Jiang, *J. Appl. Phys.*, 2008, **103**, 034119.

26 J. Q. Qi, Y. Wang, W. P. Chen, L. T. Li and H. L. W. Chan, *J. Solid State Chem.*, 2005, **178**, 279-284.

27 M. Niederberger, G. Garnweitner, N. Pinna and M. Antonietti, *J. Am. Chem. Soc.*, 2004, **126**,

9120-9126.

28 G. Xu, W. Jiang, M. Qian, X. Chen, Z. Li and G. Han, *Cryst. Growth Des.*, 2009, **9**, 13-16.

29 I. Szafraniak, C. Harnagea, R. Scholz, S. Bhattacharyya, D. Hesse and M. Alexe, *Appl. Phys. Lett.*, 2003, **83**, 2211-2213.

30 M. W. Chu, I. Szafraniak, R. Scholz, C. Harnagea, D. Hesse, M. Alexe and U. Gosele, *Nat. Mater.*, 2004, **3**, 87-90.

31 A. Roelofs, T. Schneller, K. Szot and R. Waser, *Appl. Phys. Lett.*, 2002, **81**, 5231.

32 I. Szafraniak, M. W. Chu, C. Harnagea, R. Scholz, D. Hesse and M. Alexe. *Integr. Ferroelectr.*, 2004, **61**, 231-238.

33 A. Artemev, *Philos. Mag.*, 2010, **90**, 89-101.

34 X. L. Li, B. Chen, H. Y. Jing, H. B. Lu, B. R. Zhao, Z. H. Mai and Q. J. Jia, *Appl. Phys. Lett.*, 2005, **87**, 222905.

35 M. Liu and J. Wang, *Sci. Rep.*, 2015, **5**, 7728.

36 Y. Xiao, V. B. Shenoy and K. Bhattacharya, *Phys. Rev. Lett.*, 2005, **95**, 247603.

37 L. Hong, A. K. Soh, Q. G. Du and J. Y. Li, *Phys. Rev. B.*, 2008, **77**, 94104.

38 H. H. Wu, J. Wang, S. G. Cao and T. Y. Zhang, *Appl. Phys. Lett.*, 2013, **102**, 232904.

39 H. H. Wu, J. Wang, S. G. Cao, L. Q. Chen and T. Y. Zhang, *J. Appl. Phys.*, 2013, **114**, 164108.

40 H. H. Wu, J. Wang, S. G. Cao, L. Q. Chen and T. Y. Zhang, *Smart Mater. Struct.*, 2014, **23**, 025004.

41 J. Wang and M. Kamlah, *Smart Mater. Struct.*, 2009, **18**, 104008.

42 L. Jiang, Y. Zhou, Y. Zhang, Q. Yang, Y. Gu and L. Q. Chen, *Acta Mater.*, 2015, **90**, 344-354.

43 B. L. Liu, J. B. Wang, X. L. Zhong, K. Huang, B. Li, F. Wang, J. Xie and Y. C. Zhou, *RSC Adv.*, 2014, **4**, 24533-24537

44 L. Wang, J. Wang, B. Li, X. Zhong, F. Wang, H. Song, Y. Zeng, D. Huang and Y. Zhou, *RSC Adv.*, 2014, **4**, 21826-21829.

45 L. Q. Chen, *Physics of Ferroelectrics: A Modern Perspective. Berlin, Springer-Verlag Berlin*, 2007, **105**, 363-371.

46 Unpublished data.

Table 1. Values of the normalized coefficients used in the phase field simulation[#]

α_{11}	α_{12}	α_{111}	α_{112}	α_{123}	α_{1111}	α_{1112}	α_{1122}	α_{1123}
0.62287	1.1670	0.15932	-0.24009	-0.30791	0.32152	0.21049	0.13625	0.11378
q_{11}	q_{12}	q_{44}	c_{11}	c_{12}	c_{44}	G_{11}	G_{12}	$G_{44}\,(G'_{44})$
302.96	8.3630	190.65	70943	38421	48624	0.6	0	0.3

[#] The coefficients α_{11} and α_{12} used in the phase field simulation are different from these used in the stress-free case[19] like Fig. 1, because the coefficients α_{ij} in Eq. (1) combined the contribution from the component of elastic energy to $P_i^2 P_j^2$.

Figure captions

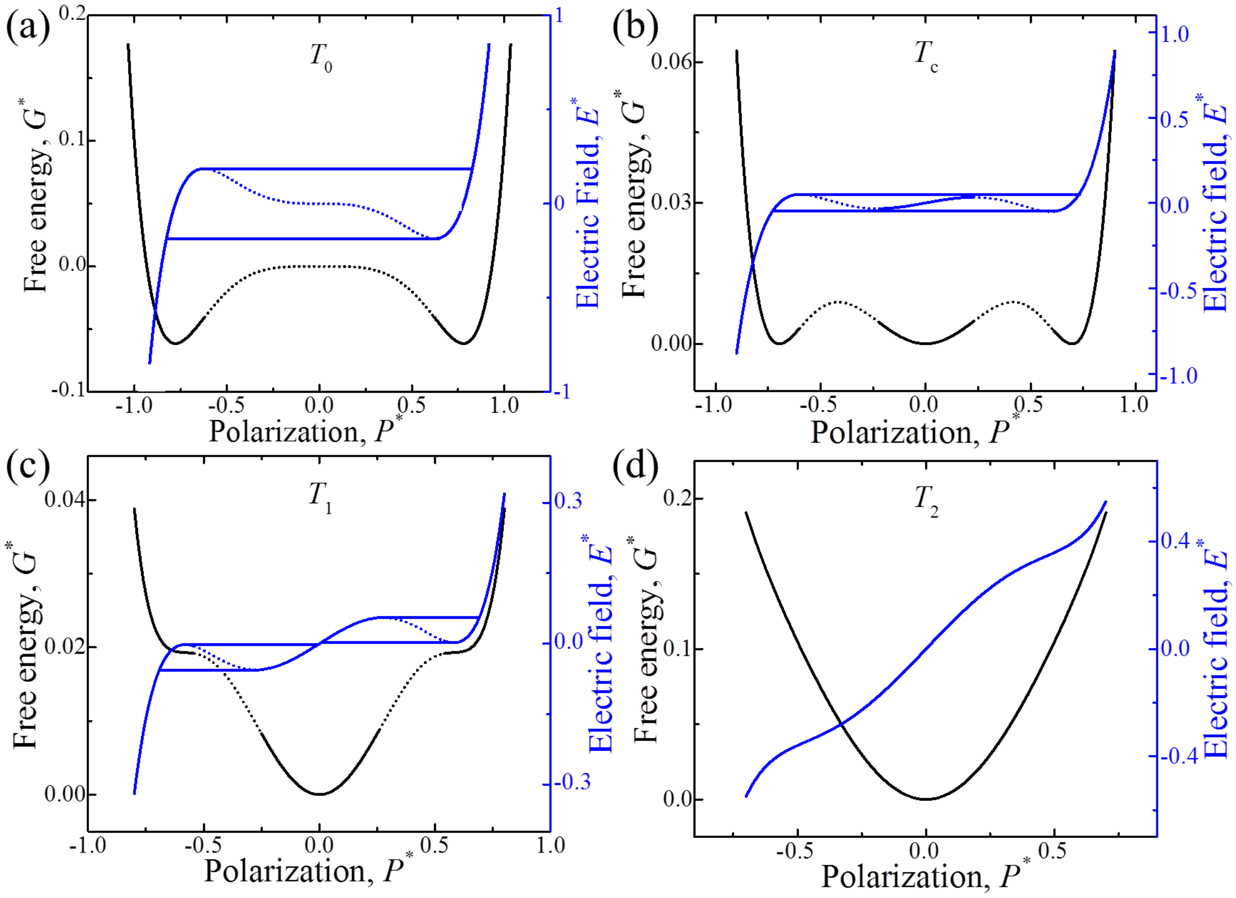

Fig. 1 Landau-Devonshire free energy and electric field versus polarization at four characteristic temperatures during the phase transition process, (a) Curie-Weiss temperature T_0 , (b) Curie temperature T_c , (c) ferroelectric limit temperature T_1 , (d) limit temperature of electric field-induced phase transition T_2 . The dotted parts of the curves correspond to the unstable state.

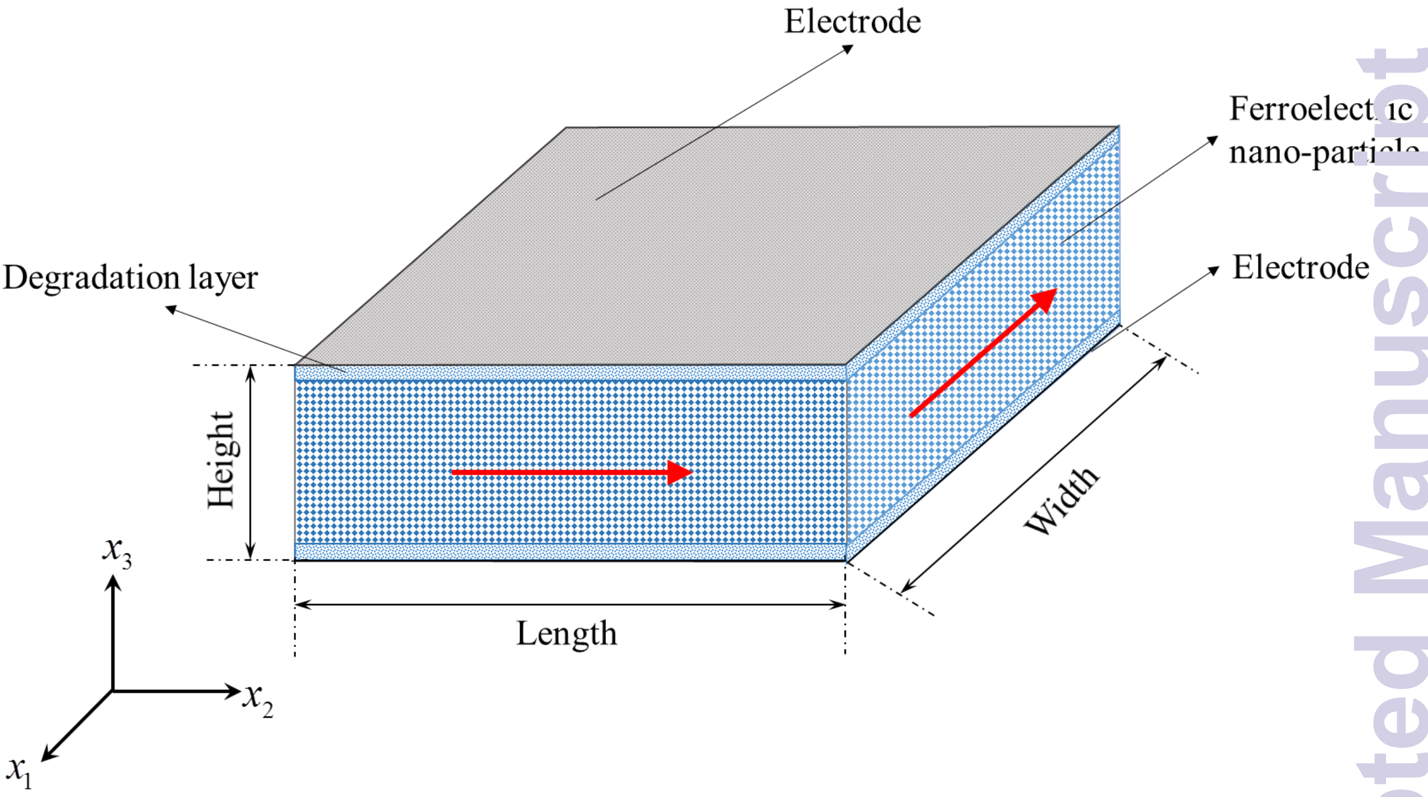

Fig. 2 A $BaTiO_3$ ferroelectric nanoparticle with two degradation layers at the upper and lower interfaces.

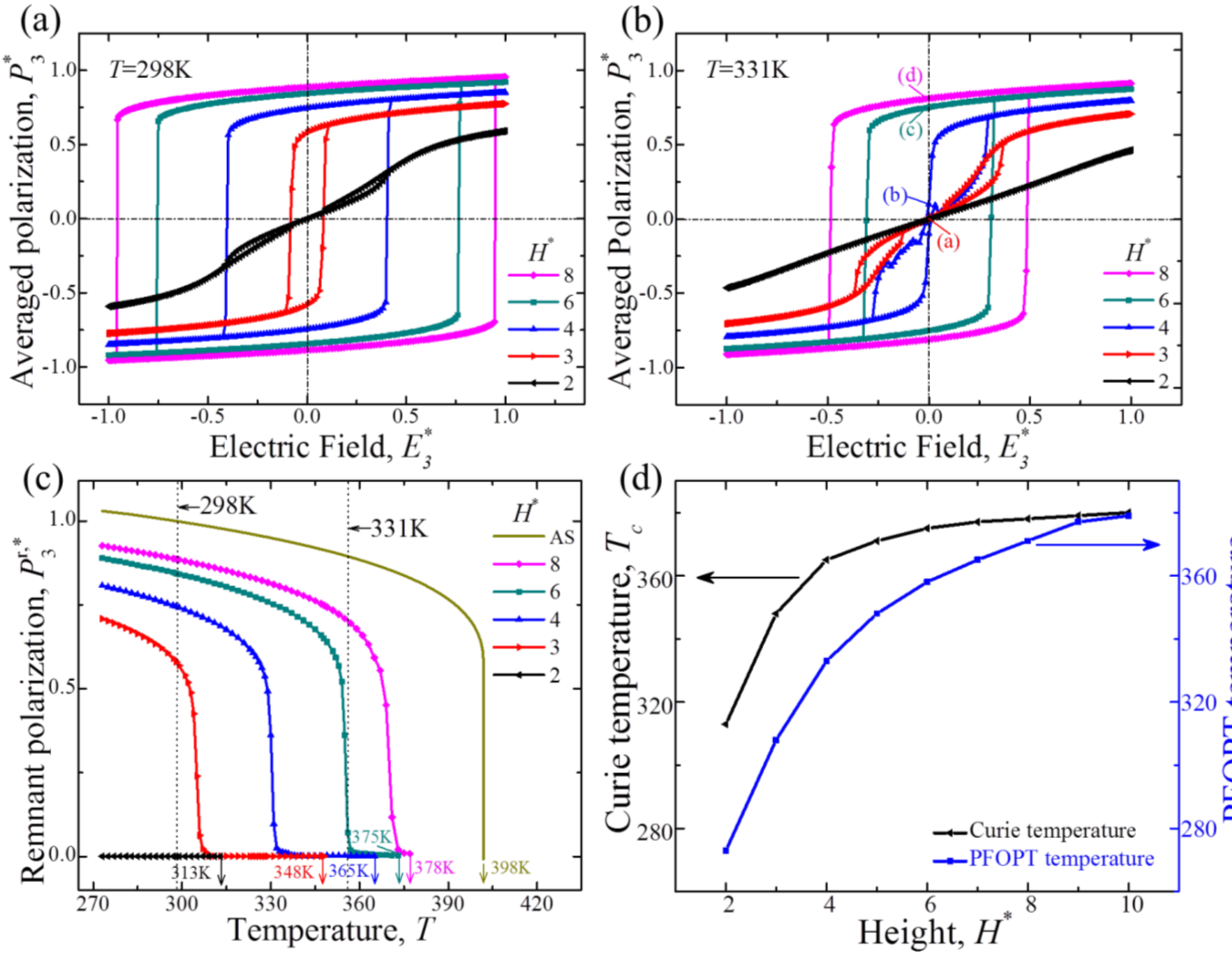

Fig. 3 Hysteresis loops of the $BaTiO_3$ nanoparticles with different height at (a) room temperature 298 K and (b) 331 K, (c) the temperature and size dependence of remnant polarization $P_3^{r,*}$, AS is the abbreviation of analytic solution, (d) the size dependence of Curie temperature T_c and PFOPT temperature.

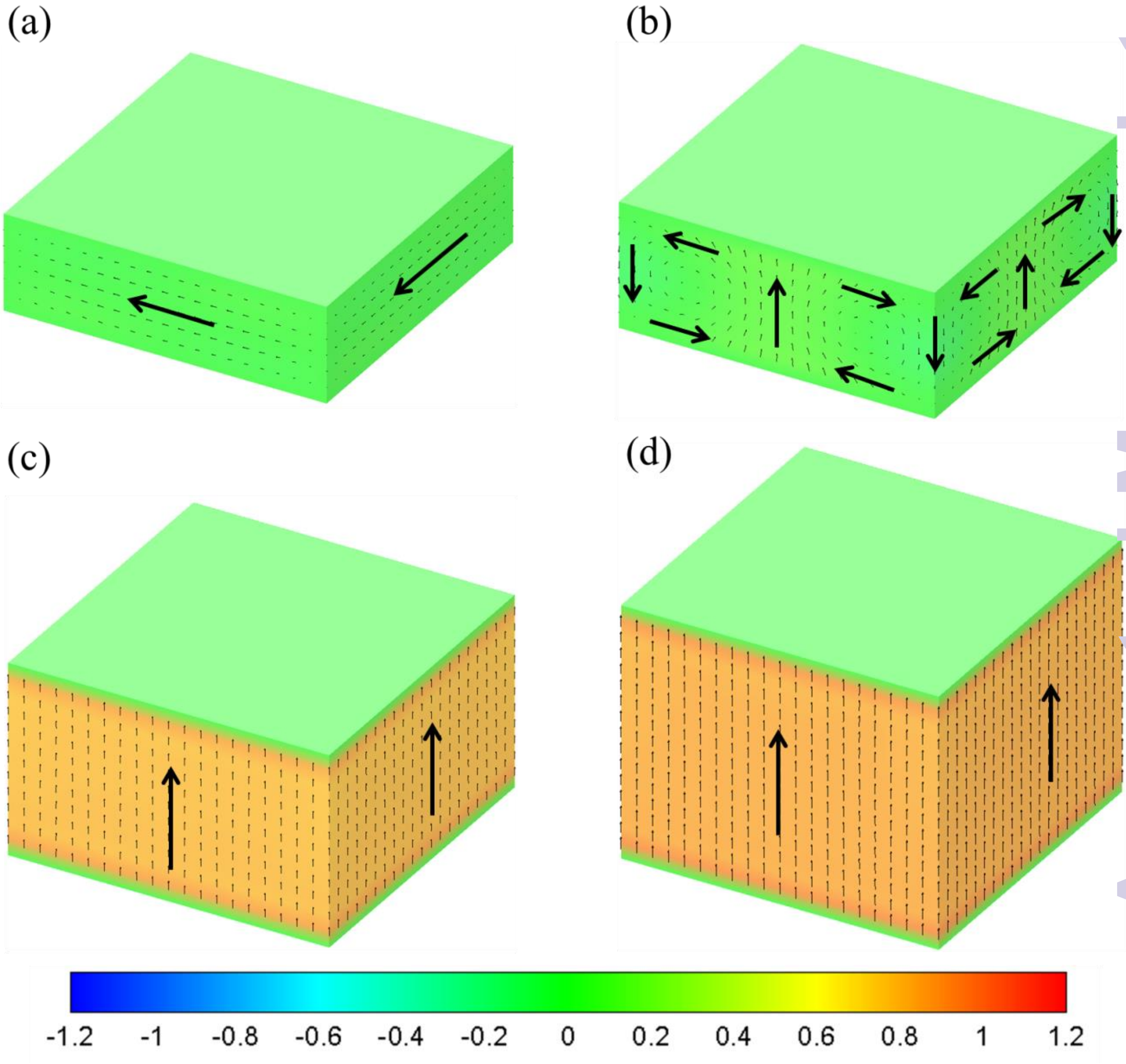

Fig. 4 Domain structures corresponding to the remnant polarizations of (a), (b), (c) and (d) in Fig. 3(b) with different nanoparticle heights: (a) $H^*=3$; (b) $H^*=4$; (c) $H^*=6$; (d) $H^*=8$ at temperature 331 K, where the applied electric field is reduced from higher values to zero.

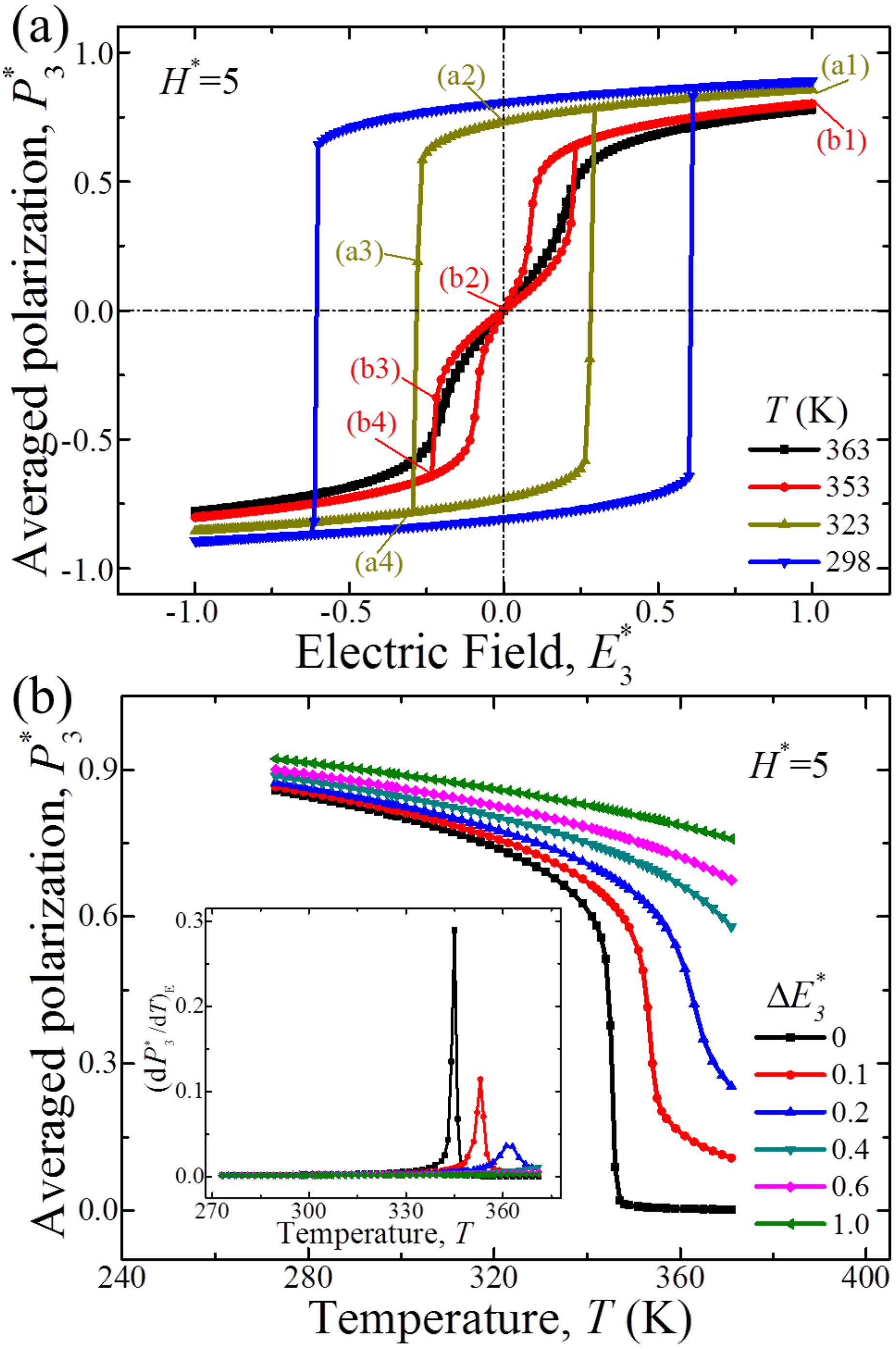

Fig. 5 (a) Hysteresis loops of the $H^* = 5$ nanoparticle at different temperatures; (b) the corresponding polarization P_3^* versus temperature, where the inset presents the corresponding $\left(dP_3^* / dT\right)_{\mathrm{E}}$.

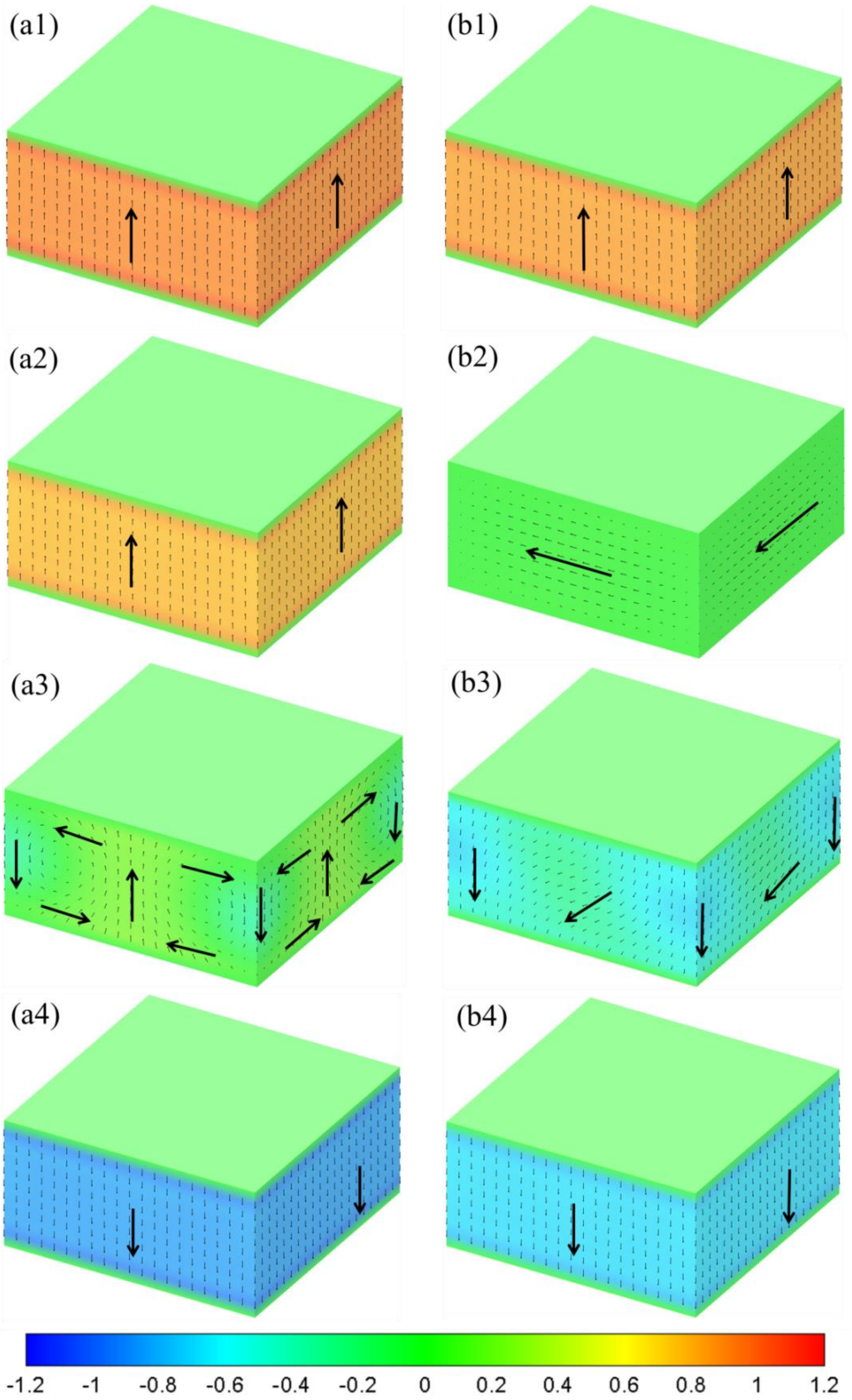

Fig. 6 Domain structures of the $H^*=5$ nanoparticles at the temperatures 323 K with respect to the applied electric field E_3^*: (a1) 1.0, (a2) 0, (a3) -0.279, (a4) -0.294; at the temperatures 353 K with respect to the applied electric field E_3^*: (b1) 1.0, (b2) 0.0, (b3) -0.218, (b4) -0.234.

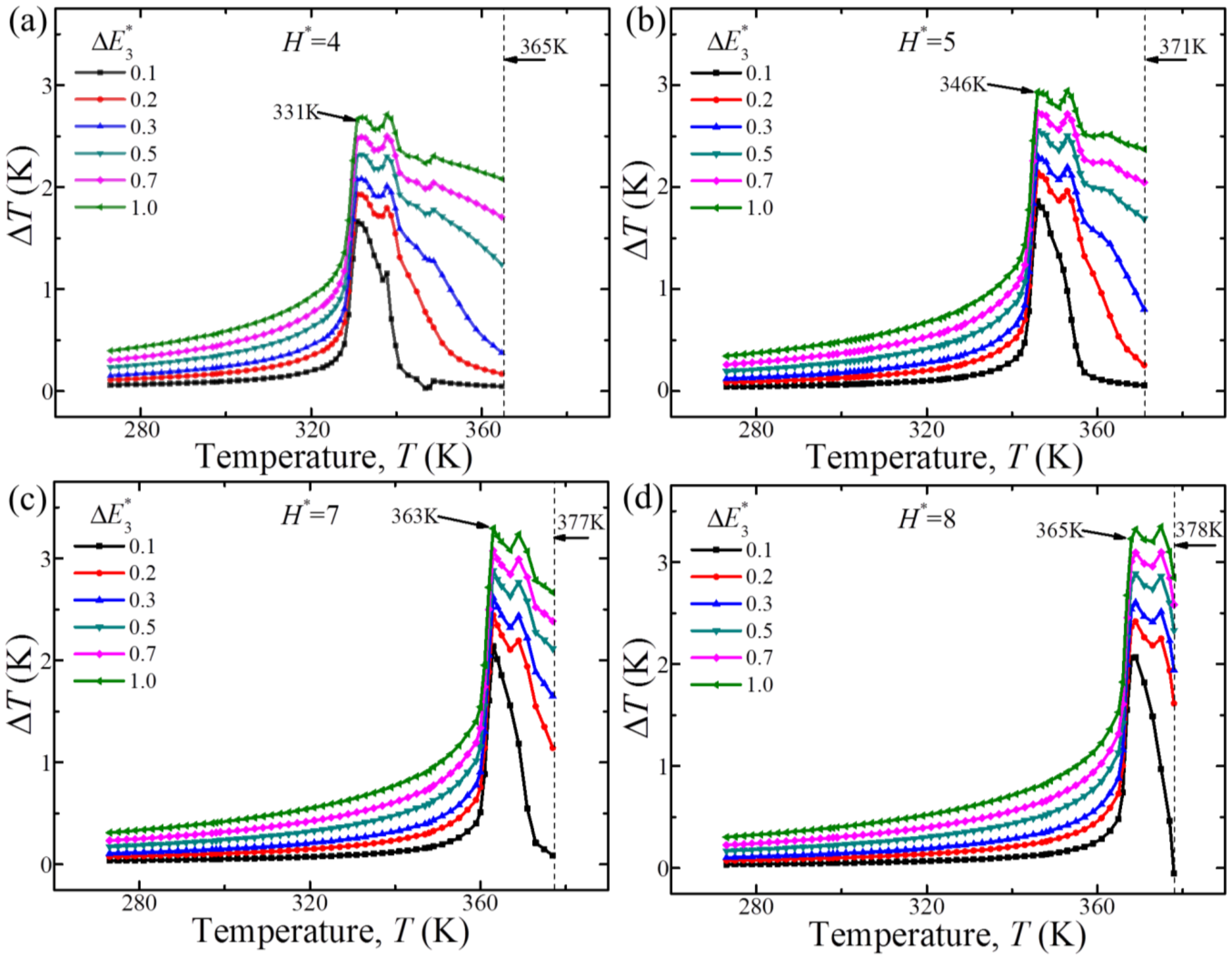

Fig. 7 ATC ΔT as a function of temperature and applied electric field of the nanoparticle height: (a) $H^*=4$ (b) $H^*=5$ (c) $H^*=7$ (d) $H^*=8$. The dashed line corresponds to its Curie temperature.

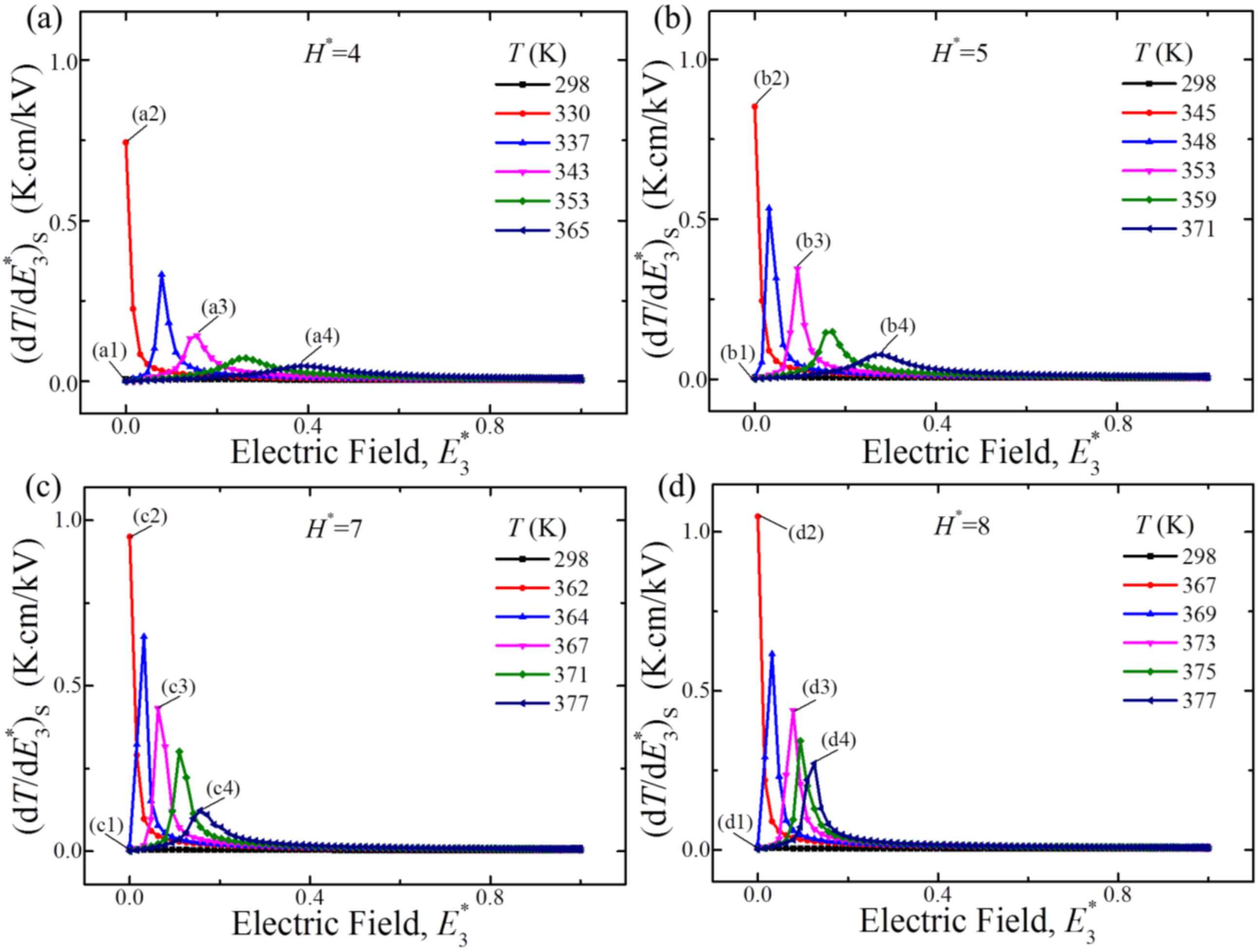

Fig. 8 Instant EC strength $(dT/dE_3^*)_S$ as a function of temperature and applied electric field of the nanoparticle height: (a) $H^* = 4$ (b) $H^* = 5$ (c) $H^* = 7$ (d) $H^* = 8$. The labels (a1)-(a4), (b1)-(b4), (c1)-(c4) and (d1)-(d4) are shown to guide the understandings.

Graphical Table of Contents

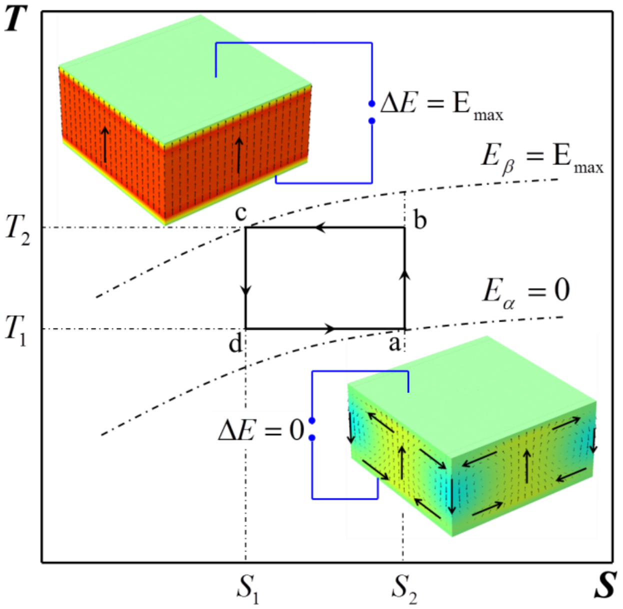

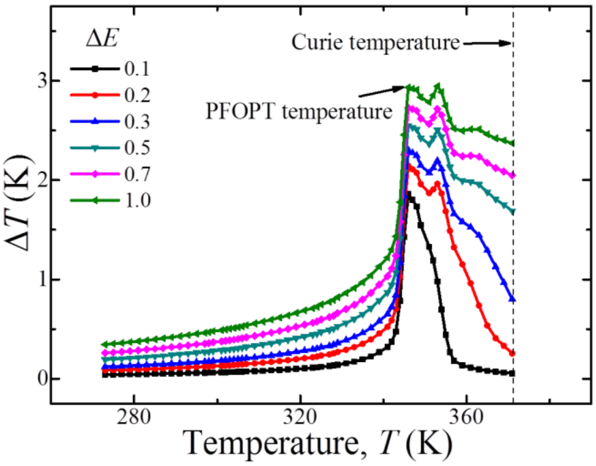

T-S diagram of one potential thermodynamic cycle for electrocaloric refrigeration (left); the proposed pseudo-first-order phase transition for ultrahigh electrocaloric effect ΔT (right)

The proposed Pseudo-First-Order Phase Transition (PFOPT) in a ferroelectric nanoparticle occurs at a temperature lower than its paraelectric/ferroelectric transition Curie temperature and is associated with ultrahigh electrocaloric effect. The PFOPT concept can be applied to all ferroelectric perovskite materials with/without the first-order paraelectric/ferroelectric transition and thus will greatly promote the application of ferroelectric nanoparticles in the next generation of solid-state cooling devices.